JGR Solid Earth

RESEARCH ARTICLE
10.1029/2019JB017831

Effects of Preexisting Structures on the Seismicity of the Charlevoix Seismic Zone

Oluwaseun Idowu Fadugba[1], **Eunseo Choi**[1], **and Christine A. Powell**[1]

[1]Center for Earthquake Research and Information, The University of Memphis, Memphis, TN, United States

Key Points:
- The CSZ seismicity and stress orientations are the combined effects of the rift faults and the impact structure
- Planar faults we considered can explain the observed seismicity but only 50% of the stress rotation
- An impact structure 4 times less elastically stiff than the surrounding crust can explain the seismicity in the CSZ

Supporting Information:
- Supporting Information S1

Correspondence to:
O. I. Fadugba,
ifadugba@memphis.edu

Citation:
Fadugba, O. I., Choi, E., & Powell, C. A. (2019). Effects of preexisting structures on the seismicity of the Charlevoix Seismic Zone. *Journal of Geophysical Research: Solid Earth*, *124*, 7370–7386. https://doi.org/10.1029/2019JB017831

Received 9 APR 2019
Accepted 4 JUL 2019
Accepted article online 8 JUL 2019
Published online 22 JUL 2019

Abstract The Charlevoix Seismic Zone (CSZ) is located along the early Paleozoic St. Lawrence rift zone in southeastern Quebec at the location of a major Devonian impact structure. The impact structure superimposed major, steeply dipping basement faults trending approximately N35°E. Approximately 250 earthquakes are recorded each year and are concentrated within and beneath the impact structure. Most *M*4+ earthquakes associated with the rift faults occurred outside the impact structure. Apart from the unique distribution of earthquakes, stress inversion of focal mechanisms shows stress rotations within the CSZ, and in the CSZ relative to the stress orientation determined from borehole breakouts. The primary goal of this research is to investigate the combined effects of the preexisting structures and regional stresses on earthquake activity and stress rotations in the CSZ. We approach this using PyLith, a finite-element code for simulations of crustal deformation. Adopting the results from recent hypocenter relocation and 3-D tomography studies, we modify the locations and dips of the rift faults and assess the effect of the new fault geometries on stress distributions. We also discuss the effects of resolved velocity anomalies. We find that the observed stress rotation is due to the combined effect of the rift faults and the impact structure. One-dimensional velocity models of the CSZ with an embedded impact structure and a combination of 65°-40°-40° and constant 70° fault dip models with a very low friction coefficient of 0.3 and cohesion of 0 MPa can explain the observed seismicity and more than 50% of the stress rotations.

1. Introduction

The Charlevoix Seismic Zone (CSZ) is the most seismically active region in eastern Canada. The CSZ is within the Late Precambrian St. Lawrence rift zone in southeastern Quebec and is overprinted by a Devonian impact structure (Figure 1). The impact structure has a radius of 28 km and is approximately 12 km deep (Rondot, 1994). The impact structure has a more damaged interior zone with a surface radius of 18 km (Figure 1). The impact structure is superimposed on three major rift faults trending N35°E and dipping to the southeast (Anglin, 1984; Rondot, 1971). The CSZ has high risk of seismic hazards due to its history of generating moderate to large earthquakes (Anglin, 1984; Lamontagne, 1999). Over 200 earthquakes are recorded each year in the CSZ (Nuttli magnitude, mN mostly ≤3; Baird et al., 2010) and the hypocenters have a bimodal distribution with peaks at 10- and 22-km depths (Vlahovic et al., 2003). The vast majority of earthquakes in the CSZ occur within the volume bounded by the rift faults (Yu et al., 2016) and those with greater magnitudes occur northeast of the impact structure (Mazzotti & Townend, 2010; Figure 1).

Vlahovic et al. (2003) conducted a three-dimensional (3-D) *P* wave velocity study of the CSZ. The tomography model shows several higher *P* wave velocity bodies at midcrustal depths. A significant fraction of the CSZ earthquakes occurs around these higher *P* wave velocity bodies, and some larger earthquakes occur along the northern edges of the high-velocity bodies.

A recent earthquake relocation and tomography study of Powell and Lamontagne (2017) using a larger number of CSZ earthquakes gives a better constraint on the geometries of these high-velocity bodies. In addition to the high-velocity bodies, Powell and Lamontagne (2017) show that the relocated earthquakes are distributed along the rift faults and thus define the geometry of the rift faults. They also conclude that the dip of the northernmost rift fault is 65°SE, while the two other major faults dip 40°SE.

Mazzotti and Townend (2010) determined the orientation of maximum principal horizontal stress (SH_{max}) from a stress inversion of focal mechanisms in 10 seismic zones in central and eastern North America including the CSZ. They found a clockwise rotation of SH_{max} in the CSZ by about 32° relative to the regional SH_{max} orientation of 54° determined from borehole breakouts (Mazzotti & Townend, 2010; Zoback, 1992). Mazzotti

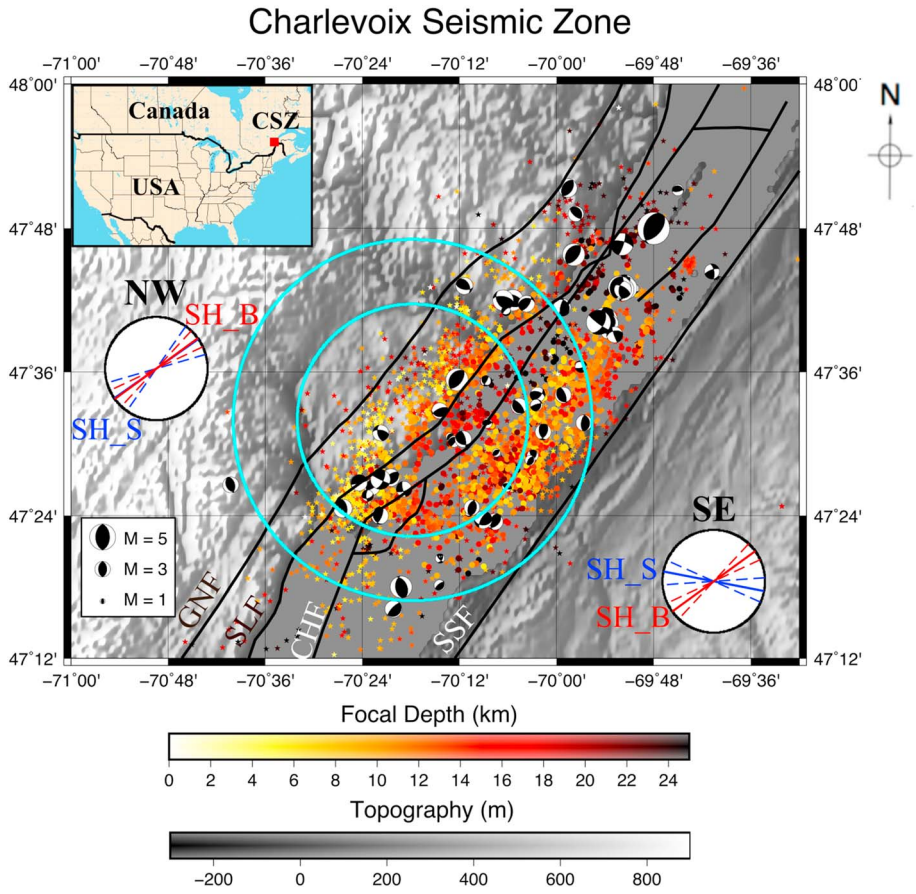

Figure 1. Topography, bathymetry, and seismicity of the Charlevoix Seismic Zone (CSZ) as well as the locations of the impact structure (outer cyan circle) and the more damaged inner impact structure (inner cyan circle). Small circles and stars are the relocated epicenters (Powell & Lamontagne, 2017) and the complete data set for the years 1988–2011, respectively, and their colors represent the focal depths. The focal mechanisms are for the earthquakes used by Mazzotti and Townend (2010) for the stress inversion. Large circles labeled as NW and SE show orientations of SH_{max} from the stress inversion of focal mechanism (SH_S) and from borehole breakout measurements (SH_B) for the earthquake clusters northwest and southeast of the impact structure center. Solid black lines mark the rift faults known in the region: GNF, Gouffre Northwest fault; SLF, Saint-Laurent fault; CHF, Charlevoix fault; and SSF, South Shore fault (Lamontagne, 1999; Rondot, 1971). The inset shows the location of the CSZ in eastern Canada. Earthquake data set is from the National Resources Canada catalog for the years 1988–2011.

and Townend (2010) observed a number of relative stress rotations in SH_{max} determined from different partitions of the earthquakes in the CSZ. The largest stress rotation occurs in the cluster of earthquakes located southeast of the impact structure midpoint relative to the earthquakes in the northwest of the impact structure midpoint. Specifically, SH_{max} in the cluster of earthquakes located southeast of the impact structure midpoint shows about a 47° clockwise rotation whereas the cluster located to the northwest has a SH_{max} that is compatible with the regional SH_{max} (Mazzotti & Townend, 2010; Figure 1).

Baird et al. (2010) explain the distribution of seismicity in the CSZ as products of the interactions between the impact structure and the rift faults. Their numerical models for the rift faults and impact structure subjected to the regional stress show increased differential stresses near the fault planes, which is consistent with the distribution of the earthquakes. Stress solutions from their numerical models show greater differential stress in the northeast of the impact structure, where most of the larger earthquakes occur, than in the southwest. However, their models could not fully explain the SH_{max} rotations in the CSZ relative to the regional SH_{max}. Instead, they addressed the observed stress rotations based on the discrepancy between the SH_{max} from the stress solutions in the seismogenic zone and the SH_{max} inverted from the modeled slips on the rift faults.

In this study, we present a new set of numerical models that can assess the impacts of stress distribution due to fault geometry, frictional strengths of faults, elastic properties of the impact structure and velocity models

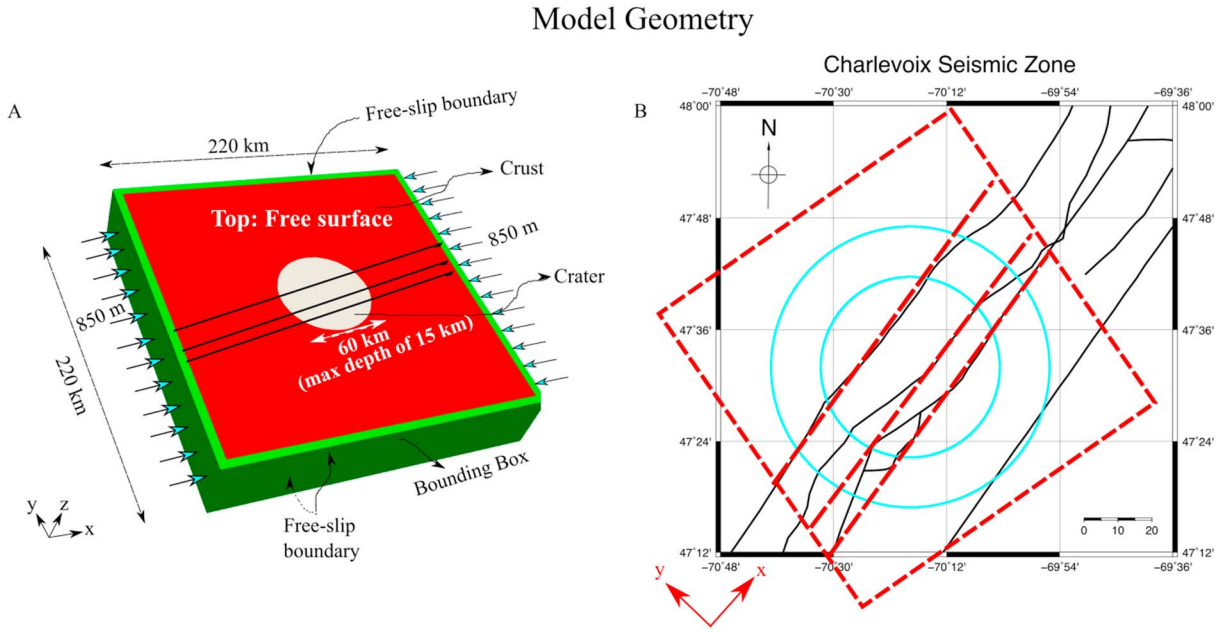

Figure 2. (a) Model domain with the impact structure (gray) and crust (red). The three rift faults (black lines), dimensions, boundary conditions and the total amount of displacement are annotated. The outer 10-km-thick layer of crust (green) is added to contain fault edges within the domain, a requirement by PyLith. (b) The orientation of the model domain (red dotted box) and the associated coordinate axes (red arrows) relative to the geographic reference frame. The red dotted box is not the actual model domain but just a box that shows its "orientation." Cyan circles on the geographic map show the inner and outer impact structure boundaries and black solid lines trace rift faults (see Figure 1).

for the region. We then try to correlate modeled stress distributions with the recently-relocated hypocenters (Powell & Lamontagne, 2017) and discuss implications for the nonuniform stress orientation around the impact structure that was previously recognized.

2. Model Setup

We create numerical models that include three major rift faults and the damaged impact structure (Figure 2a). For this purpose, we use PyLith version 2.1.0 (Aagaard et al., 2013; Aagaard et al., 2015), an open-source finite-element code for modeling dynamic and quasi-static tectonic deformation. PyLith is suitable for the intended models because it can compute elastic responses of a model involving multiple faults and material heterogeneities subjected to various types of loading.

2.1. Model Geometry

Our models are composed of three units, crust, impact structure, and rift faults, reflecting a simplification of the geology of the region (Figure 2a). The crust is a 220- × 220- × 40-km box with the impact structure cut out. The impact structure is modeled as a spherical cap with a surface diameter of 60 km and a depth of 15 km.

The three rift faults have a strike of N35°E and are embedded in the crust layer except for the top surface edge that is exposed on the surface. The three faults correspond to the Gouffre NW River, St. Laurent, and the Charlevoix faults (Figure 1). Baird et al. (2010) modeled the Gouffre River, St. Laurent, and the South Shore faults. They did not model the Charlevoix fault. The locations of the rift faults relative to the impact structure are based on geologic maps by Lamontagne (1999) and Rondot (1971). We create two sets of models with different dip angles of the faults based on two proposed geometries of the rift faults. One set has a uniform dip of 70°SE for all three faults (Anglin, 1984; Baird et al., 2010), while the other has 65°, 40°, and 40° for the three planar faults, from north to south, respectively (Powell & Lamontagne, 2017).

We conducted resolution tests in which the change in displacement and stress solutions relative to a 1-km-resolution model are monitored as a function of element size. Displacements and differential stresses do not change appreciably for elements sizes equal to 4 km or smaller (Figure S1 in the supporting information). Based on the resolution tests, we use the element size of 2 km for most of the models and 4 km

Table 1
List of Numerical Models

Model	Velocity model	Dip of rift faults	Moduli ratio	μ[a]	C[a](MPa)	K[a,b](MPa)	G[a,b](MPa)
SNFR25	Saguenay Region[c]	No faults	0.25	0.3	0	55.7	32.7
SD70R25		70°-70°-70°	0.25	0.3	0	55.7	32.7
SD70R25V		70°-70°-70°	0.25	0.1–0.6	0	55.7	32.7
SD65R25		65°-40°-40°	0.25	0.3	0	55.7	32.7
SD70R50		70°-70°-70°	0.5	0.3	0	55.7	32.7
SD70R100		70°-70°-70°	1.0	0.3	0	55.7	32.7
LD70R25	1-D Model[d]	70°-70°-70°	0.25	0.3	0	60.0	35.7
TD70	Tomography[e]	70°-70°-70°	–	0.3	0	58.7	35.3

[a]μ, C, K, and G are friction coefficient, cohesion, bulk and shear modulus, respectively. [b]K, G at 10-km depth. [c]Somerville et al. (1990). [d]Lamontagne (1999). [e]Powell and Lamontagne (2017).

for more computationally expensive models like those for exploring the effects of the friction coefficient. Low-friction models, especially those with μ equal to 0.1 and 0.2, are very expensive due to slow convergence rate in the nonlinear solution scheme. Running all the models in this group at the same mesh resolution of 4 km ensures intragroup consistency; and the comparison with 2-km-resolution models is also justified because the descritization error does not significantly increase as the resolution increases to 4 km (Figure S1). We also observe edge effects by comparing a 420- × 420- × 40-km model with the original 220- × 220- × 40-km model, finding that the seismogenic parts around the impact structure show consistent displacement and stress solutions for both domain sizes. Based on this result, we choose the smaller domain for this study and set the element size to be about 2 km. The average computation time was about 16 days for fault models ($\mu = 0.3$) with 2-km element size on 16 cores on the University of Memphis High Performance Computing cluster. The model with fault dips of 65°-40°-40° took about 2 times as long to run for the same model time. We do not clearly understand why the model with shallower-dipping faults is slower than the others roughly by a factor of 2 and further analyzing computational efficiency is beyond the scope of this paper.

2.2. Initial and Boundary Conditions

Initial stresses are assumed to be lithostatic but due to the nonplanar geometry of the impact structure, computing initial lithostatic equilibrium stresses is not trivial. We first compute lithostatic stresses based on the density distribution from an adopted velocity model for the CSZ (Table 1) and use it as an initial stress distribution. We then use this stress solution as the true initial stress conditions. We verify that this two-step approach leads to an initial stress field perfectly balancing the gravitational body force by observing that the initial vertical displacements are uniformly zero.

Velocities are prescribed on the sides perpendicular to the x axis (Figure 2a) while the y perpendicular sides and the bottom boundary are free-slip and the top boundary is traction-free. Rather than applying velocities oblique to the sides, we rotate the model domain such that the x axis is oriented to N55°E, the regional SH_{max} direction (Zoback, 1992) (Figure 2b). We apply a 1 m/yr compressive velocity in the x axis direction. The magnitude of boundary velocity does not represent any tectonic loading in the continental interiors but has the sole purpose of increasing the differential stress ($\sigma_D = \sigma_1 - \sigma_3$). Noting that the depth distribution of earthquakes within the impact structure has a peak at 10 km (Baird et al., 2010; Powell & Lamontagne, 2017), we increase the boundary displacement until σ_D reaches 706 MPa at 10-km depth based on Byerlee's law for dry rocks, $\tau = 50$ MPa $+0.6\,\sigma_n$ (Byerlee, 1978). More details of the full derivation of the stopping criterion for boundary loading is given in the supporting information. We assume that σ_3 corresponds to the lithostatic stress and adopt the sign convention that compressive stress is negative.

2.3. Elastic Moduli From Velocity Models

We assume linear elasticity for both crust and impact structure. To obtain elastic moduli and density distributions, we consider three regional velocity models and one recent model based on local earthquake tomography (Powell & Lamontagne, 2017). The regional models are for the Saguenay region in Quebec (Somerville et al., 1990), the 1-D standardized half-space velocity model of eastern Canada (Lamontagne, 1999), and the 1-D velocity model derived from a simultaneous inversion of hypocenters and velocities of the CSZ (Lamontagne, 1999) (Figure 3).

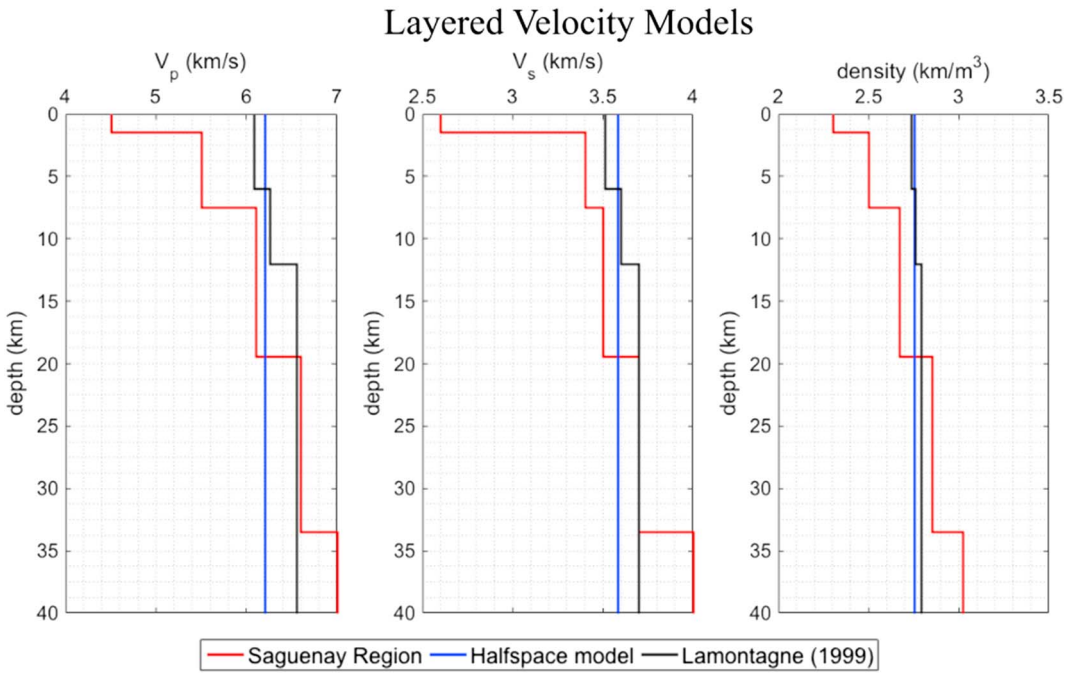

Figure 3. Velocity models used in this study. Red, blue, and black lines are velocity models for the Saguenay region (Somerville et al., 1990), the Geological Survey of Canada (GSC) standard velocity model of Eastern Canada (Lamontagne, 1999), and the Canadian Shield (North Shore) velocity model of Charlevoix Seismic Zone (Lamontagne, 1999).

We also consider a nonuniform distribution of density and elastic moduli inferred from the 3-D V_p and V_s tomography model by Powell and Lamontagne (2017), of which V_p and V_s variations for the depth range from 12 to 14 km are shown in Figure 4. The tomography has a block size of 2 km, and velocity features with a dimension of 6 km can be resolved. Since this tomography solution does not cover the entire study area, we assume a half-space velocity model (Lamontagne, 1999) outside of the tomography coverage. Smooth transition between the tomography model and the half-space model is achieved by linear interpolation. Densities (ρ) are computed according to Gardner's principle (Gardner et al., 1974): $\rho = 0.31V_p^{0.25}$, where V_p is the P wave velocity in meters per second and density is given as grams per cubic centimeter.

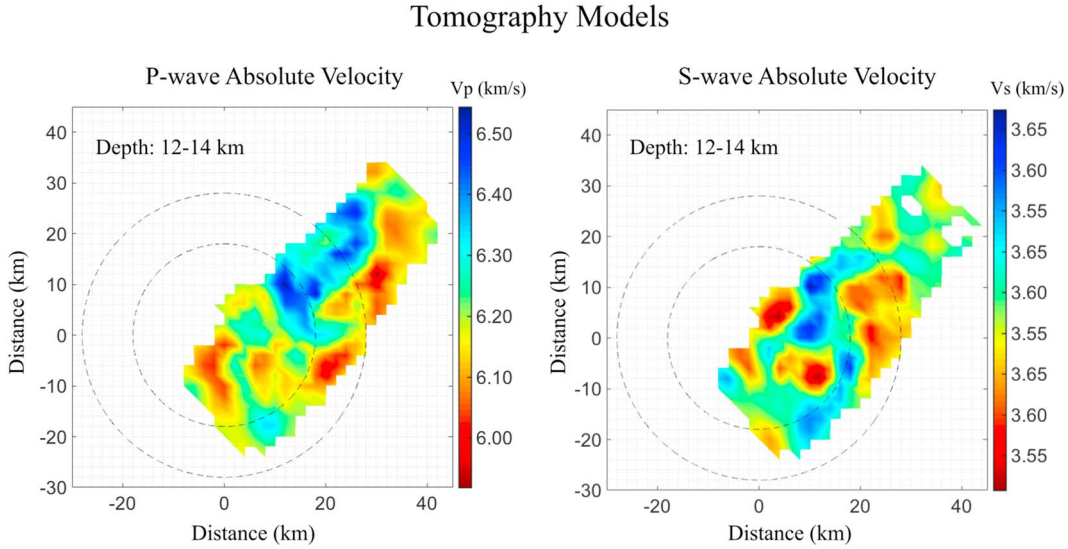

Figure 4. Variation of (left) V_p and (right) V_s at the depths from 12 to 14 km from the 3-D seismic tomographic model by Powell and Lamontagne (2017).

For simplicity, we assume that the impact structure's bulk and shear moduli are a certain fraction of those of the crust (e.g., Baird et al., 2010). Similarly, the density of the impact structure is reduced from that of the 1-D velocity models over the corresponding depth range to model damaged crustal rocks. Models with density reduced by 0 to 20% were run but did not exhibit significant changes as shown in Figure S3 in the supporting information. All the models presented in this study have 10% of density reduction in the impact structure.

2.4. Treatment of Rift Faults

We treat the rift faults as cohesive-frictional planes, on which slip vectors are not prescribed but determined by the model. In order to create relative motions across the rift fault planes, PyLith decouples the motion of the two sides of the faults by inserting cohesive cells on the fault surfaces. We assign a coefficient of static friction (μ) and the cohesion (C) on the fault. We assume that μ and C are uniform on the fault planes in each model but investigate the consequences of varying μ from 0.1 to 0.6 at a constant C of 0 MPa. Although cohesion values from 0 to 30 MPa have been tested and found to have significant effects, we choose to present models with zero cohesion in this study because it is appropriate for preexisting faults with low normal stress (e.g., Marone, 1995). We note that the deep portions of the model faults might not satisfy the condition of low normal stress and thus a further investigation on the depth-variation of cohesion is desirable.

The reference model (SNFR25) has the geometry described above but without the rift faults. This is equivalent to a model with infinitely strong faults. The initial stress state is close to the initially assumed lithostatic stress after the nonplanar correction due to the impact structure. We determine the percentage change in differential stress, $\Delta\sigma'_D = 100(\sigma_D - \sigma_{D,\mathrm{ref}})/\sigma_{D,\mathrm{ref}}$, and the change in the orientation of $\mathrm{SH_{max}}$, $\Delta\phi_{\mathrm{max}} = \phi_{\mathrm{max}} - \phi_{\mathrm{max,ref}}$, where ϕ_{max} denotes the orientation of the maximum principal stress (σ_1). Since our model domain was rotated clockwise about the center of the impact structure by 35°, ϕ_{max} equal to zero should be understood as parallel to the regional stress field. Positive and negative values of ϕ_{max} correspond to anticlockwise and clockwise rotation from the direction of applied loading, respectively. In order to quantify the spatial correlation between the simulated stress changes and the earthquake hypocenters, we determine the percentage of hypocenters that fall within the region of $\Delta\sigma'_D \geq 0.5\%$. We did not account for the uncertainty in hypocenter relocation and the effect of any along-strike variation in the fault dips.

2.5. Control Parameters

We create a series of models in which the following parameters are varied: dips of the rift faults, friction coefficients, impact structure-crust elastic moduli ratios, and the velocity models. Two fault geometries for the CSZ are considered. One model has a dip angle of 70°SE for all three rift faults (Baird et al., 2010). The other assumes that the three faults have dip angles of 65°SE, 40°SE, and 40°SE from north to south (Powell & Lamontagne, 2017).

Impact structure-crust elastic moduli ratios tested are 0.25, 0.5, and 1.0. When the modulus ratio is 1.0, the impact structure has the same velocity model as the crust. The friction coefficient, μ, is varied from 0.1 to 0.6 at a constant cohesion of 0 MPa in one set of models. We assume that μ and C are the same for the three rift faults and it is uniform on the fault planes, including the part of the faults within the impact structure region.

Three velocity models are considered in this study: The 1-D Saguenay velocity model (Somerville et al., 1990), the 1-D CSZ velocity model (Lamontagne, 1999), and the 3-D V_p and V_s tomography model (Powell & Lamontagne, 2017; Figures 3 and 4). When the tomography model is used, the impact structure-crust moduli ratio becomes irrelevant. All the models presented in this paper are listed in Table 1.

3. Results

3.1. Reference Model (SNFR25)

The effects of the weaker impact structure are dominant in SNFR25. σ_D is smaller by hundreds of megapascals in the impact structure region relative to the surrounding crustal rock as shown by 5- and 10-km-depth sections (Figure 5a). The absolute value of σ_D is greater (i.e., is more negative) in the direction perpendicular to the applied loading than in the parallel direction. At depths below the impact structure (i.e., depths ≥15 km), σ_D is more negative at the central region by about 300 MPa relative to the average σ_D at those depths (Figure 5a). The higher negative value of σ_D at 15-km depth decreases to the average value at that depth within 20 km from the center of the model geometry. The effect of the impact structure weakens at 20 km and eventually becomes insignificant at 25 km (Figure 5a).

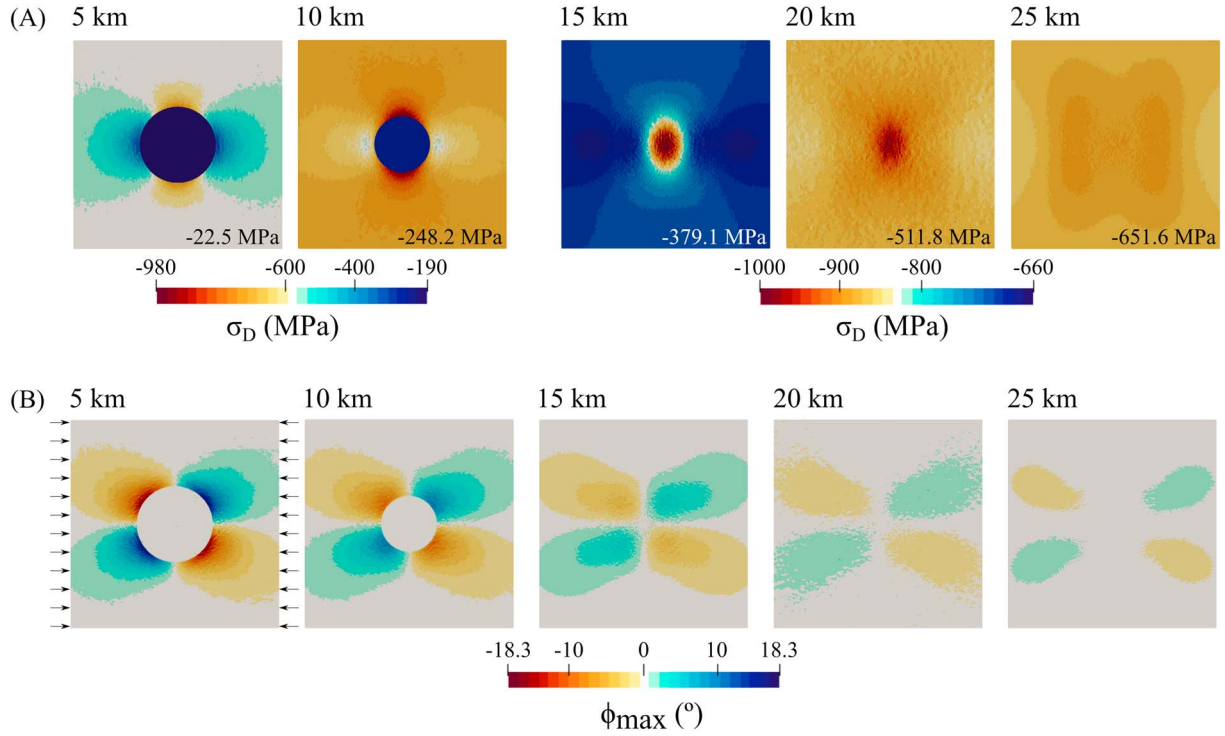

Figure 5. (a) Differential stress (σ_D) and (b) SH_{max} orientation (ϕ_{max}) in the reference model (SNFR25) at different depths. The value of lithostatic stress at each depth is at the lower right corner of each depth slice in Figure 5a. The arrows in Figure 5b represent the loading direction for all models. Note the change in scale in Figure 5a for depths greater than 10 km. Each figure is 70 × 70 km.

The ϕ_{max}, the orientation of SH_{max}, shows a four-lobe pattern of alternating polarities around the impact structure (Figure 5b). The ϕ_{max} uniformly approaches 0°, the loading direction, away from the impact structure and also with depth (Figure 5b). In the SE corner of the impact structure, ϕ_{max} shows a maximum clockwise (i.e., negative) rotation of about 18.3° from the regional stress direction (5-km panel in Figure 5b). The ϕ_{max} at 5- and 10-km depths is close to 0° within the impact structure, being subparallel to the regional stress orientation (Zoback, 1992).

3.2. Effects of Rift Faults and Their Dip

3.2.1. SD70R25

Magnitudes of σ_D in SD70R25 are smaller in the impact structure than in the surrounding crust, as in the reference model but also significantly modified by abrupt changes in the vicinity of the rift faults (Figure 6a). The σ_D at a distance greater than 50 km from the center of the impact structure is similar to that of the reference model at each depth.

The ϕ_{max} shows a four-lobe pattern of alternating polarities around the weaker impact structure, but modifications made by the faults are also clearly visible. The ϕ_{max} in the surrounding crust approaches 0° as distance from the impact structure's center or depth increases (Figure 6b). The ϕ_{max} within the impact structure is about −5° at a depth of 5 km but is subparallel to the regional stress orientation at 10-km depth (Figure 6b). The main effect of the rift faults is a 5° to 15° ϕ_{max} clockwise rotation that persists along the faults at 5- and 10-km depths. The sense of near-fault ϕ_{max} rotations flips to anticlockwise at 10 km within the impact structure and at depths below the impact structure in the surrounding crust. The anticlockwise rotation also persists along the faults and has a magnitude of about 5°.

The distribution of positive $\Delta\sigma'_D$ values, corresponding to increased differential stresses in SD70R25 relative to SNFR25, spatially overlaps with the seismicity in general and particularly well at 10 km (Figure 6c). About 70% of the hypocenters fall in the region with $\Delta\sigma'_D \geq 0.5\%$. We superimpose the relocated hypocenters of earthquakes of Powell and Lamontagne (2017) that occurred within 2 km of each depth slice. The hypocenters are rotated clockwise by 35° about the center of the impact structure in order for them to be

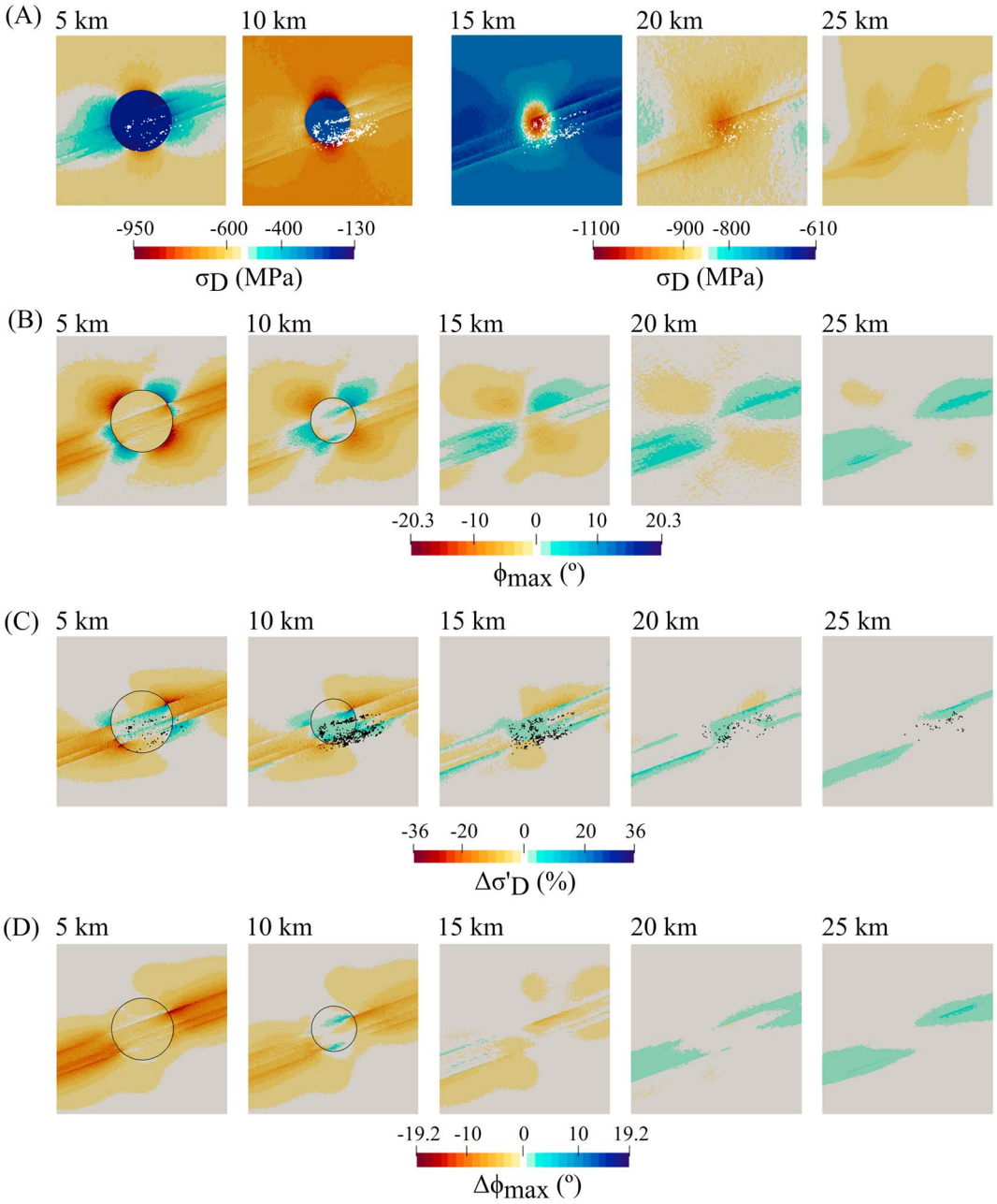

Figure 6. (a) Differential stress (σ_D), (b) SH_{max} orientation (ϕ_{max}), (c) percentage change in differential stress ($\Delta\sigma'_D$), and (d) the change in ϕ_{max} ($\Delta\phi_{max}$) in SD70R25 model relative to SNFR25 at various depths. Note the change in scale in Figure 6a for depths greater than 10 km. Earthquakes within 2 km of each depth slice are represented by black dots in Figure 6c. The outline of the impact structure is represented as a black circle. Each figure is 70 × 70 km.

consistent with the rotated model geometry. Some earthquakes fall in the region of negative $\Delta\sigma'_D$ near the SW and NE boundary of the impact structure at depths shallower than 15 km.

The $\Delta\phi_{max}$ maps in Figure 6d show that the rift faults rotate SH_{max} of SNFR25 further clockwise at 5- and 10-km depths by up to 19°. The effect of clockwise rotation due to the faults is diminished within the impact structure and flips the sense of rotation to anticlockwise at 10 km (Figure 6d). At depths below the impact structure, the overall impact of the faults decrease everywhere.

Three vertical cross sections of $\Delta\sigma'_D$ from the SD70R25 model are shown in Figure 7. As marked on the 10-km-depth slice of $\Delta\sigma'_D$ (left panel in Figure 7), they are all perpendicular to the fault strike. Two cross

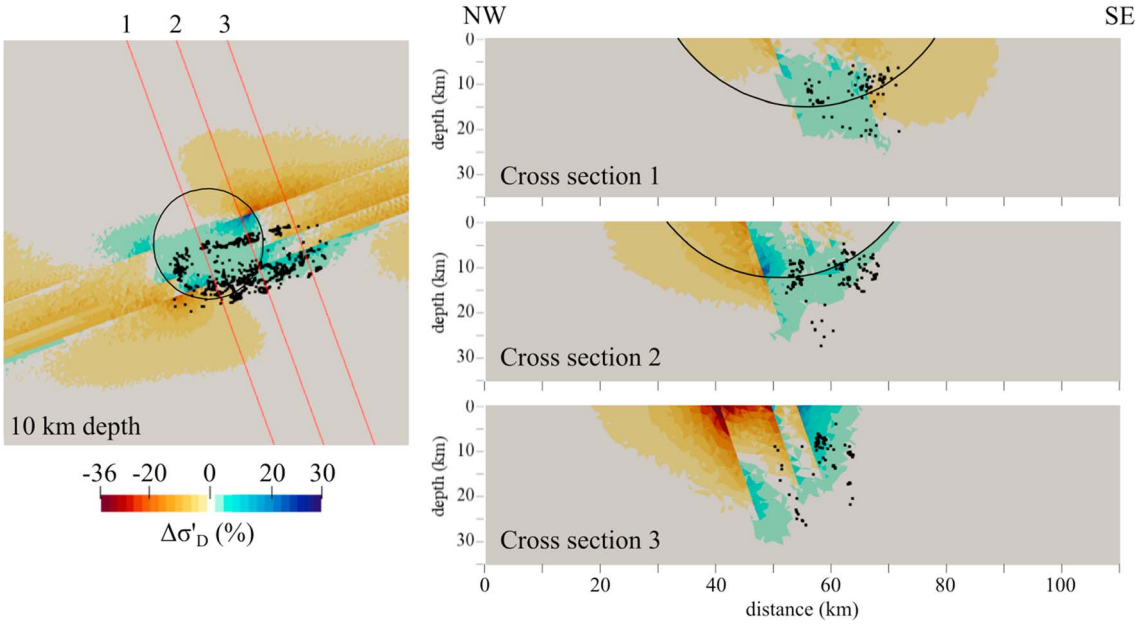

Figure 7. NW-SE cross sections through the percentage change in differential stress ($\Delta\sigma'_D$) solution in the SD70R25 model. Earthquakes within 2 km of each cross section are represented by black dots. The three NW-SE cross sections are indicated on the 10-km-depth slice showing earthquakes within 2 km of the depth slice. The outline of the impact structure is represented as black circle and curved lines on the depth slice and cross sections, respectively. The depth slice is 70 × 70 km centered on the impact structure. Note the cross sections have the same color and length scales as the depth slice in Figure 7a.

sections, 1 and 2, go through the central and marginal areas of the impact structure but the cross section 3 does not intersect the impact structure. Also plotted on these cross sections are the hypocenters of the region's earthquakes within 2 km from each cross section. Most of the earthquakes fall within regions of increased differential stress but some are associated with negative or negligible changes in differential stress. In the cross sections going through the impact structure, the broad region between the northernmost and the southernmost fault shows positive $\Delta\sigma'_D$. In contrast, the relocated hypocenters exhibit well-defined linear trends as observed by Powell and Lamontagne (2017).

3.2.2. SD65R25

Correlation between the $\Delta\sigma'_D$ distribution in SD65R25 and the observed seismicity is not as clear as in SD70R25 but shows more fine-scale correlation with the observed seismicity, especially at 10-km depth (Figure 8). At 15-km depth, the region of positive $\Delta\sigma'_D$ correlates with the earthquakes on the northernmost fault but the earthquakes on the middle rift fault fall in regions with negative $\Delta\sigma'_D$.

Greater clockwise rotations of SH_{max} are found in SD65R25 than in SD70R25 at all depths (Figure 8) although both models show the four-lobe pattern and magnitudes of ϕ_{max} decreasing with depth. Within the impact

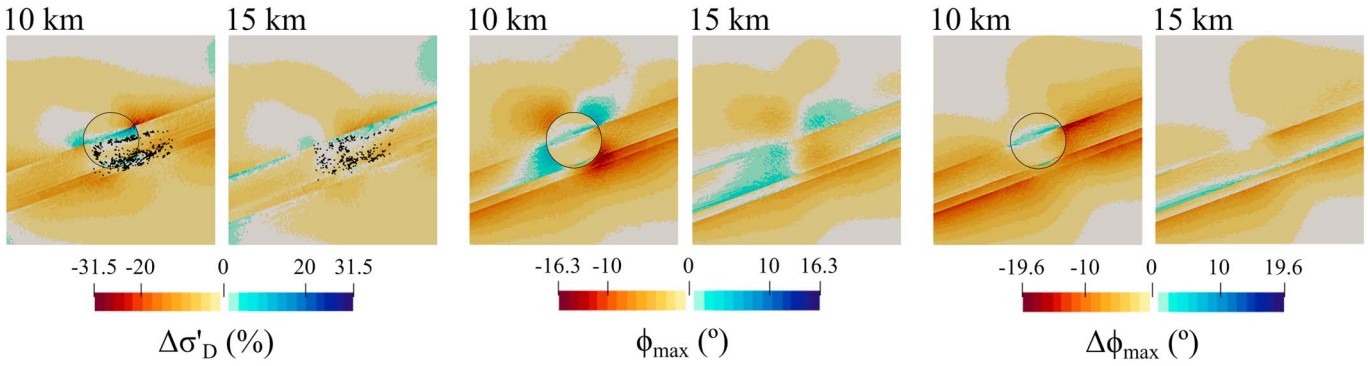

Figure 8. Percentage change in (left) differential stress ($\Delta\sigma'_D$), (middle) SH_{max} orientation (ϕ_{max}), and the (right) change in ϕ_{max} ($\Delta\phi_{max}$) at 10- and 15-km depths from the SD65R25 model. Earthquakes within 2 km of each depth slice are represented by black dots in Figure 8a. The outline of the impact structure is represented as a black circle. Each figure is 70 × 70 km.

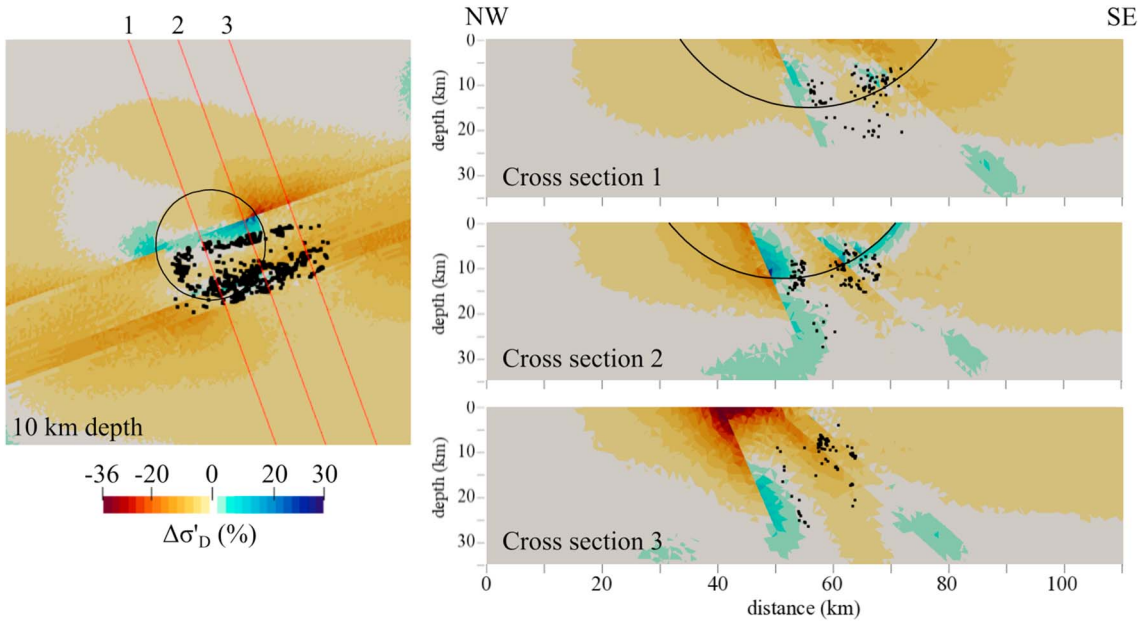

Figure 9. Same as Figure 7 but for SD65R25 model.

structure, SD65R25 shows clockwise rotations of about 5° at 10-km depth and the counterclockwise rotation observed for model SD70R25 is seen only north of the northernmost fault because the other two faults barely cross the impact structure region at this depth due to their shallower dip (Figure 8). In the surrounding crust close to the rift faults, ϕ_{max} rotates clockwise by 5° to 16.3° relative to the regional stress direction (Figure 8). Counterclockwise rotation of ϕ_{max} relative to the regional SH_{max} extends to the northeast and southwest of the impact structure in the fault-bounded region.

When compared to SH_{max} orientations in the reference model, SD65R25 shows greater clockwise rotations of ϕ_{max} by up to 20° near the rift faults and the northeastern boundary of the impact structure at 10-km depth (Figure 8). These values of $\Delta\phi_{max}$ are greater than those of SD70R25 and thus can be attributed to the shallower dips of the faults in SD65R25.

The region of increased differential stress in SD65R25 exhibits well-defined linear trends near the rift faults, and thus gives a better explanation for the narrow and well-defined seismicity near the impact structure (Figure 9). About 25% of the hypocenters fall in the region with $\Delta\sigma'_D \geq 0.5\%$. The SD65R25 model shows a region of negative $\Delta\sigma'_D$ between the observed seismicity on the northernmost and southernmost faults. The earthquakes on the middle rift fault and most of the earthquakes on the southernmost fault outside the impact structure fall in regions with negative $\Delta\sigma'_D$ (Figure 9).

3.3. Effects of the Weakness of the Damaged Impact Structure Zone

Two models with the rift faults dipping at 70° are constructed such that the ratio of elastic moduli of the impact structure to that of the surrounding crust are 0.5 (SD70R50) and 1.0 (SD70R100), respectively.

3.3.1. SD70R50

While the effects of the impact structure and rift faults are still clear and consistent, SD70R50 values of $\Delta\sigma'_D$ are mostly negative with some exceptions at 10-km depth amounting to about a 10% increased stress (Figure 10a). The region of positive $\Delta\sigma'_D$ in the SD70R50 model overlaps with the hypocenters only in the southeast corner of the impact structure boundary and the southernmost rift fault (i.e., the Charlevoix fault) at 5-km depth, amounting to about 45% of the hypocenters in the region with $\Delta\sigma'_D \geq 0.5\%$ (Figure 10a). The spatial correlation of seismicity with increased σ_D relative to the reference model is stronger at 10-km depth.

The ϕ_{max} plots show the four-lobe pattern of alternating polarities and shows the effects of the rift faults. The maximum value of ϕ_{max} is about 13° (Figure 10a). The $\Delta\phi_{max}$ maps in Figure 10a show that the rift faults rotates the ϕ_{max} in the reference model at 5- and 10-km depths up to 16.5°. The value of $\Delta\phi_{max}$ decreases to almost zero at 15-km depth and is anticlockwise up to −3° at 20- and 25-km depths.

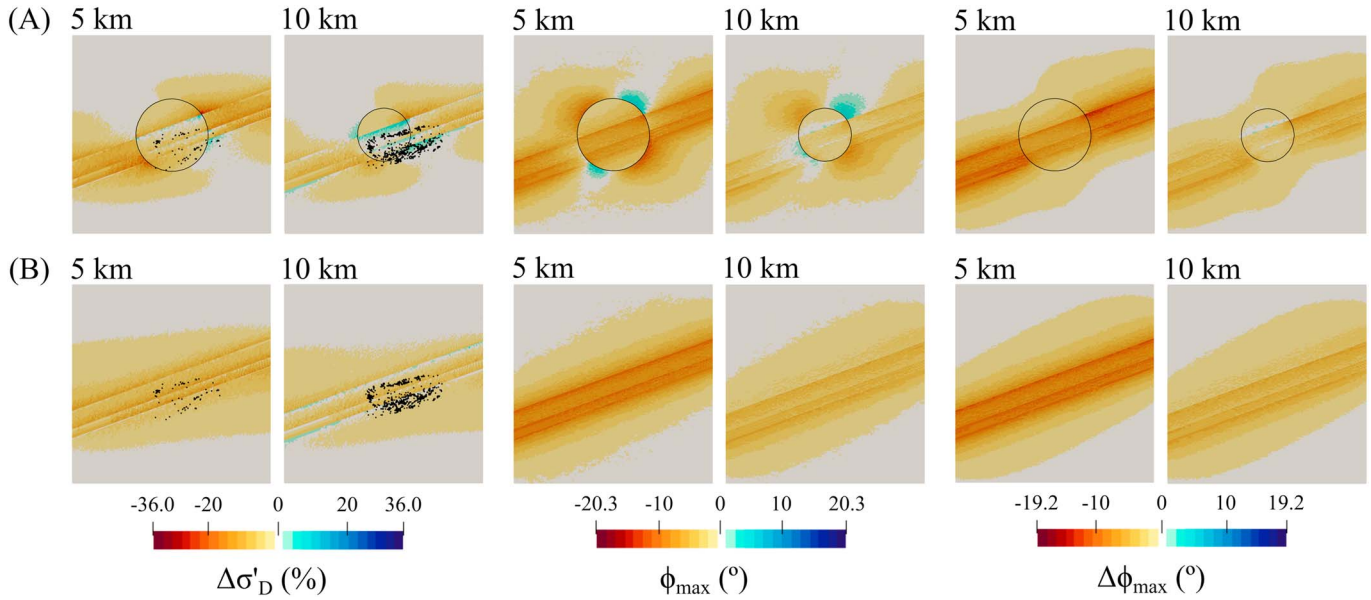

Figure 10. Same as Figure 8 but for the models with different impact structure-crust elastic moduli ratios: (a) SD70R50 and (b) SD70R100.

3.3.2. SD70R100

The $\Delta\sigma_D'$ and ϕ_{max} only exhibit the effects of the rift faults since the impact structure and the crust have the same elastic moduli in model SD70R100 (Figure 10b).

Positive $\Delta\sigma_D'$ values in SD70R100 are seen only at a depth of 10 km, and their distribution does not fit the observed seismicity (Figure 10b). About 23% of the hypocenters fall in the region with $\Delta\sigma_D' \geq 0.5\%$. The $\Delta\sigma_D'$ correlates with observed seismicity below 15 km except for some earthquakes in the northern cluster. However, the model predicts earthquakes throughout the entire length of the rift faults at and below 15-km depth. Figures that show all the depth slices are in the supporting information (Figure S4). The result of a model with an intermediate moduli ratio of 0.75 is somewhat between the SD70R50 and SD70R100 models (Figure S5).

The distribution of ϕ_{max} values lacks the four-lobe pattern and is negative in the vicinity of the rift faults at 5- and 10-km depth: that is, ϕ_{max} values are rotated clockwise relative to the regional SH_{max} (Figure 10b). The values of ϕ_{max} range from 2° (25-km depth) to 12.8° (5-km depth). The ϕ_{max} decreases to 0° at about 50 km from the center of the model along the direction perpendicular to the fault strike.

The maximum value of $\Delta\phi_{max}$ is 12.8° and, being indistinguishable from ϕ_{max}, signifies that the $\Delta\phi_{max}$ values in SD70R100 are controlled by the rift faults (Figure 10B). The value of $\Delta\phi_{max}$ decreases to almost zero at 15 km depth, and becomes anticlockwise in the fault region at 20 and 25 km.

3.4. Effects of Fault Strength (SD70R25V)

We compute σ_D and ϕ_{max} in a series of models in which the rift faults dip at 70° but their friction coefficient (μ) is varied systematically at a constant cohesion of 0 MPa. We assume that the fault parameters are the same for each rift fault and uniform throughout the fault surfaces. The parameter μ varies from 0.1 to 0.6 with an interval of 0.1. We use a mesh resolution of 4 km for SD70R25V models due to the expensive computation time at μ values of 0.1 and 0.2. Aside from the change in the friction coefficient and the mesh resolution, the six models computed are the same as SD70R25. $\Delta\sigma_D'$ and ϕ_{max} computed for these models are plotted in Figure 11, which shows 10-km depth sections because of the high number of earthquakes within 2 km from that depth.

Magnitudes of $\Delta\sigma_D'$ decrease as μ increases (Figure 11A) because the model behaviors must approach those of the no-fault model as fault strength increases. When μ values are 0.1 and 0.2, the area of positive $\Delta\sigma_D'$ regions does not cover the entire observed seismicity, with about 3% and 24% of the hypocenters within the region of $\Delta\sigma_D' \geq 0.5\%$, respectively. The regions of positive $\Delta\sigma_D'$ for μ values equal to 0.3 and 0.4 show better spatial correspondence with the seismicity of the CSZ. However, the model with $\mu = 0.4$ predicts positive

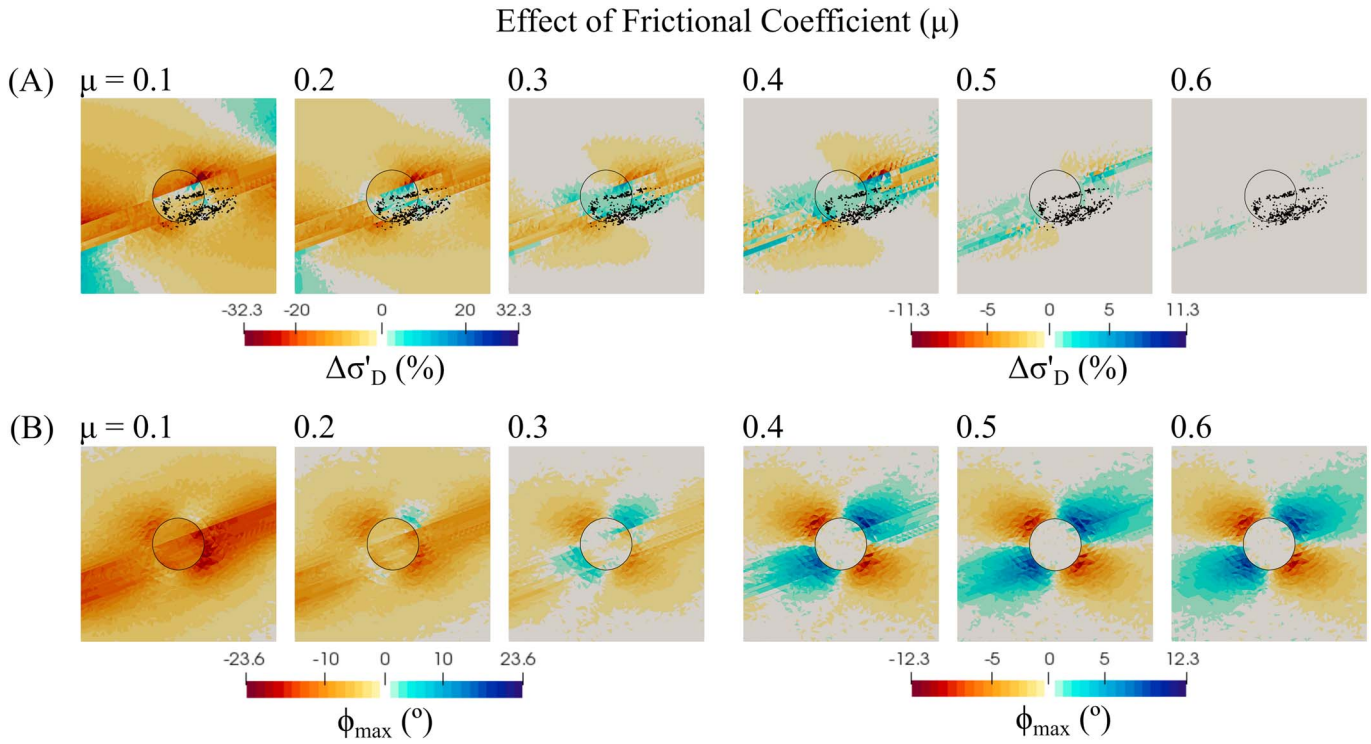

Figure 11. Effect of friction coefficient on the $\Delta\sigma'_D$ and ϕ_{max} in the SD70R25V model at 10-km depth. Note the change in scale for μ greater than 0.3. Earthquakes within 2 km of each depth slice are represented by black dots in Figure 11a. The outline of the impact structure is represented as a black circle. Each figure is 70 × 70 km.

Coulomb stress changes along the entire length of the rift faults, which is contrary to the limited spatial extent of the observed seismicity. Also, about 66% of the hypocenters in the model with $\mu = 0.3$ fall within the region of $\Delta\sigma'_D \geq 0.5\%$ while only 35% do when $\mu = 0.4$. However, when the hypocenters falling in the region with $\Delta\sigma'_D \geq 0\%$ are considered, the percentages increase to 73% and 82% for μ equal to 0.3 and 0.4. The $\Delta\sigma'_D$ approaches zero when μ values are 0.5 and 0.6, for which the faults are locked. The percentage of hypocenters in the region with $\Delta\sigma'_D \geq 0.5\%$ reduces to 1.4% and 0% when μ values are 0.5 and 0.6, respectively.

The ϕ_{max} maps show a clockwise stress rotation in the entire seismic zone, including the impact structure region, when μ values are 0.1 and 0.2 (Figure 11B). When μ is 0.3, ϕ_{max} is subparallel to the regional stress orientation within the impact structure region and the four-lobe pattern appears. For $\mu \geq 0.4$, the distribution of ϕ_{max} approaches that of the reference model.

3.5. Effects of Velocity Models

LD70R25 and TD70 are the same as SD70R25 except that they use different velocity models. We use the 1-D velocity model (Lamontagne, 1999; Figure 3) and the 3-D tomography results (Powell & Lamontagne, 2017; Figure 4) in LD70R25 and TD70 models, respectively. The V_p and V_s tomography model covers and extends beyond the impact structure region, so the impact structure-crust elastic moduli ratio is irrelevant because it is dictated by the velocities.

3.5.1. LD70R25

Despite the difference in the 1-D velocity models of Lamontagne (1999) and Somerville et al. (1990) especially at depths shallower than 20 km (Figure 3), the results of LD70R25 are similar in spatial distribution and in magnitude to those of SD70R25 (Figure 12a). Regions of positive $\Delta\sigma'_D$ spatially overlap with the observed seismicity at all depths and especially well at 10-km depth (Figure 12a).

The ϕ_{max} maps also show the four-lobe pattern around the weaker impact structure and modification of the ϕ_{max} by the rift faults is observed (Figure 12a). The maximum value of ϕ_{max} is 21.7° and decreases to 12.4° at 10-km depth. The $\Delta\phi_{max}$ map shows that the rotation of the reference model ϕ_{max} due to the rift faults is up to 10.8° at 10-km depth (Figure 12a).

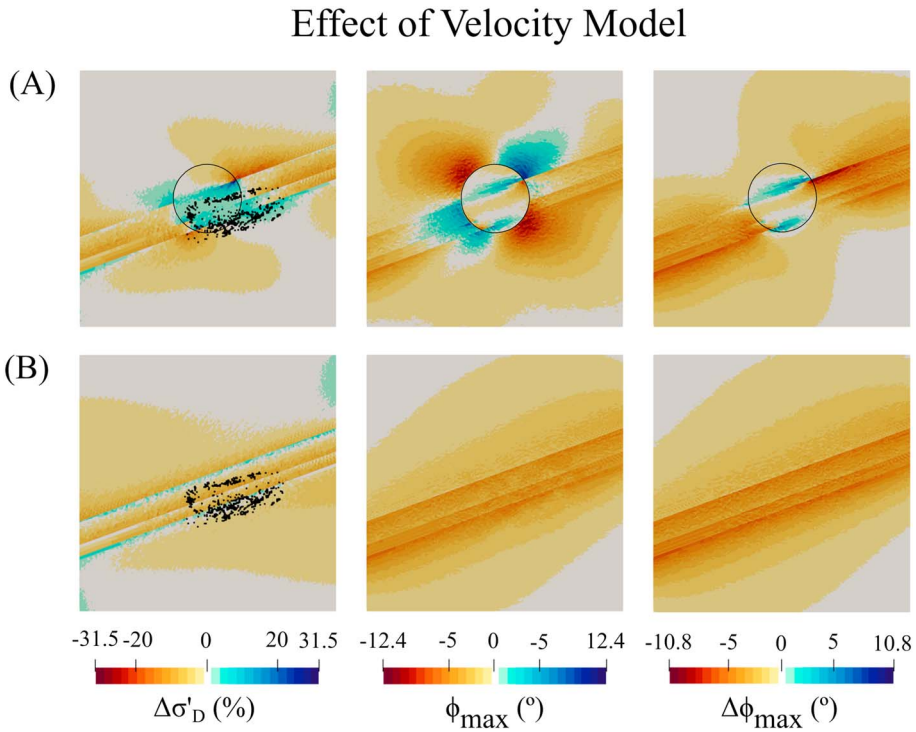

Figure 12. Same as Figure 8 but only at a depth of 10 km for (a) LD70R25 and (b) TD70.

3.5.2. TD70

TD70 shows very different results from those of the models with a layered velocity model and a weak impact structure. As the tomography model does not clearly show low velocities within the impact structure region, $\Delta\sigma'_D$, ϕ_{max} and $\Delta\phi_{max}$ are all very similar to those in SD70R100, in which the impact structure is not distinguished from the surrounding crust in terms of elastic stiffness.

The spatial correlation between $\Delta\sigma'_D$ and the observed seismicity is poor, especially at 10-km depths (Figure 12b). Below 15-km depths, the earthquakes fall within a region of positive $\Delta\sigma'_D$, but the modeled distribution of $\Delta\sigma'_D$ predicts earthquakes throughout the entire length of the rift faults.

The ϕ_{max} maps do not show the characteristic four-lobe pattern as seen in the models with the impact structure due to the lack of a significant decrease in the velocity model within the impact structure versus outside the impact structure (Figure 12b). The ϕ_{max} maps show a clockwise rotation relative to the regional stress orientation up to 12.4° at 10-km depth (Figure 12b).

The $\Delta\phi_{max}$ is similar in magnitude and in spatial distribution with the ϕ_{max} maps (Figure 12b). This similarity in magnitude shows that the stress rotations in TD70 model are due to the presence of the rift faults.

4. Discussions

4.1. Earthquake Distribution

Our models suggest that having both the rift faults and the impact structure is not only sufficient but also necessary for explaining the distribution of earthquakes in the CSZ. The models without a weaker impact structure zone, SD70R100 and TD70, show regions of positive $\Delta\sigma'_D$, a proxy for earthquake generation potential, along the entire length of the rift faults (e.g., Figure 10b). In contrast, when the impact structure is set to be elastically softer than the surrounding crust by up to a factor of 4, positive $\Delta\sigma'_D$ regions spatially coincide with the observed seismicity in the CSZ, especially above 15-km depth (e.g., Figure 6c). Our models predict that earthquake activity should extend to about 20-km distance from the impact structure in a northeast direction (Figure 6c). This distribution of positive $\Delta\sigma'_D$ is not seen in the reference model without the rift faults. These two findings from our models are consistent with the conclusion drawn by Thomas and Powell (2017) that the seismicity in CSZ requires both the damaged impact structure zone and the rift faults.

The SD70R25 and SD65R25 models can explain the seismicity of the CSZ at least partially (Figures 7 and 9). Correlation between the $\Delta\sigma_D'$ distribution in SD65R25 and the observed seismicity shows a better and fine-scale correlation than in SD70R25, especially well near and within the impact structure region (Figure 9), while those in SD70R25 fit the observed seismicity better in the northeast region outside the impact structure (Figure 7). These differential correlations with seismicity of positive $\Delta\sigma_D'$ regions in SD70R25 and SD65R25 might be suggesting along-strike variations in the dip angles of the rift faults (e.g., Baird et al., 2010). The SD65R25 model explains the observed seismic gap between the NW and SE clusters (i.e., between Gouffre Northwest and the Saint-Laurent faults, Figure 1) and can also explain the rimming of earthquakes around the impact structure as noted by Powell and Lamontagne (2017) especially at 10-km depth (Figure 9).

Our present models, however, cannot explain the differences in earthquake activity between the impact structure and the surrounding crust in the CSZ. The "b" values of the Gutenberg-Richter relationship for the regions within and outside the impact structure are 0.93 and 0.74, respectively (Yu et al., 2016), indicating a higher frequency of small magnitude earthquakes within the impact structure. Also, most *M*4+ earthquakes in the CSZ appear to occur in the northeast region outside the impact structure (e.g., Baird et al., 2010; Lamontagne, 1999; Powell & Lamontagne, 2017). Reexamination of historical earthquakes in the Charlevoix area by Stevens (1980) shows that some *M*4+ earthquakes in the period 1924–1978 also occurred at the SE end of the impact structure. Our models do not show significantly higher values of $\Delta\sigma_D'$ in the seismogenic zone outside the impact structure relative to the regions within the impact structure (Figure 6c). A possible explanation is that faults created in the highly fractured impact structure region (Rondot, 2000) might have lower friction coefficients than the faults outside the impact structure. Stress buildup on those weaker impact structure faults can be quicker and smaller in magnitude than on faults outside the impact structure under the same tectonic loading, resulting in more numerous, smaller magnitude earthquakes within versus outside the impact structure.

4.2. Spatial Variations of SH_{max} Orientation

Stress orientations in the CSZ from focal mechanism stress inversions (Mazzotti & Townend, 2010; Zoback, 1992) show relative clockwise rotations within the CSZ and in the CSZ relative to the regional stress orientation. A clockwise rotation of about 47° is observed in the SE relative to NW clusters of earthquakes and about 32° from the stress inversion of the entire CSZ earthquakes relative to the SH_{max} determined from borehole breakouts (Mazzotti & Townend, 2010; Zoback, 1992; Figure 1).

Most of the earthquakes in the NW cluster are within the impact structure region and occur at about 10-km depth (Figure 1). Our model shows that the rift faults tend to rotate the stress orientation clockwise in the upper 15-km depth but the amount of rotation is reduced within the weak impact structure (e.g., Figure 6d). However, the model with an impact structure-crust moduli ratio of 1.0 shows significant clockwise rotations uniformly along the entire length of the rift faults (Figure 10b). This observation suggests that the impact structure tends to align the ϕ_{max} to the regional tectonic loading direction within the impact structure, particularly at 10-km depth (Figure 6d).

In a model with a impact structure and the rift faults (SD70R25), the stress rotation in the CSZ is clockwise (maximum value of 20.3°) and decreases to 0° at an average of 20 km away from the CSZ (Figure 6b). SD70R25 can explain about 60% of the 32° clockwise stress rotation observed in the CSZ relative to the borehole breakouts, and about 43% of the 47° rotation in the SE part of the CSZ relative to the NW part. The magnitudes of ϕ_{max} in the SD65R25 model are higher than the SD70R25 model by 6° but show a small clockwise rotation within the impact structure at 10-km depth, and thus can explain about 80% of the 32° clockwise stress rotation observed in the CSZ relative to the borehole breakouts and about 55% of the 47° rotation in the SE part of the CSZ relative to the NW part. The increase in ϕ_{max} in the SD65R25 relative to the SD70R25 models suggests that the remaining observed stress rotations, not explained by either model, could be partly due to change in dip angle of the rift faults with depth.

A clockwise stress rotation of about 44° relative to the stress orientation from borehole breakouts is also observed in the Lower St. Lawrence seismic zone (Mazzotti & Townend, 2010). The Lower St. Lawrence seismic zone is located along the St. Lawrence River to the NE of the CSZ and does not contain an impact structure, similar to the SD70R100 model. The rotation suggests that the presence of the rift faults and the relative angles of their strikes with respect to the regional orientation of SH_{max} alone can result in stress rotations (e.g., Zoback, 1992). However, the combined effect of the impact structure with up to a quarter of

the elastic moduli of the surrounding crust and the rift faults are required in the CSZ to explain the observed clockwise rotations of the ϕ_{max} in the SE cluster of earthquakes relative to the NW cluster, as well as in the entire CSZ relative to the direction of regional tectonic loading.

4.3. Frictional Strengths of the Rift Faults

The surface expression of the rift faults used in this study corresponds to the Gouffre Northwest fault, Saint-Laurent fault, and Charlevoix fault (Figure 1). We did not consider the South Shore fault given its aseismic nature, although it appears to mark a boundary to the active zone (Lamontagne, 1999). Our models show that a μ of 0.3 and cohesion values of 0 MPa create $\Delta\sigma_D'$ maps that spatially correlate with the seismicity of CSZ and the observed stress rotations (Figure 11). We ran a series of models in which the rift faults dip at 70° and the friction coefficient (μ) is fixed to be 0.3 while cohesion (C) is one of 0, 3, 5, 10, 20, and 30 MPa (Figure S6). Cohesion values less than 5 MPa could better explain the spatial distribution of observed seismicity in the CSZ than the greater values. μ equal to 0.4 also seems suitable to the rift faults as the $\Delta\sigma_D'$ maps spatially correlate well with the seismicity of the CSZ. A small number of earthquakes also occurred at the SW region outside the impact structure (Figure 1).

The fault parameters in our study are not compatible with the analysis of Hurd & Zoback (2012a, 2012b) who suggest normal values of μ (0.6–0.8) for the rift faults and hydrostatic pore pressure. Also, Fereidoni and Atkinson (2014) use Coulomb stress theory to investigate stress change in the CSZ caused by the 1,663 earthquake (moment magnitude M of 7) and conclude that the rift faults are strong with μ of 0.8. Fereidoni and Atkinson (2014) showed that decreasing the apparent coefficient of friction reduces the spatial correlation of the regions with enhanced stress and observed seismicity. Specifically, μ values of 0.2 and 0.4 give 66% and 75% spatial correlation, respectively. However, in our model, the regions of positive $\Delta\sigma_D'$ significantly decrease in spatial extent when μ is 0.6 and do not fit the observed seismicity in the CSZ (Figure 11).

In our study, we stop increasing boundary displacements when σ_D reaches 706 MPa at 10-km depth as described earlier without making any assumptions for the intermediate principal stress (σ_2). In contrast, Baird et al. (2010) used a σ_D equal to 200 MPa at 10-km depth as their stopping criterion for boundary loading. They suggested that the rift faults in the CSZ are very weak with a μ of about 0.1. The higher stopping criterion in our study is based on Byerlee's law under the assumption of no pore fluid pressure on the rift faults, and it is necessary to make faults slip at seismogenic depth when μ is 0.3 as assumed in this study. Inclusion of pore fluid pressure can significantly reduce the magnitude of σ_D used as the stopping criterion. In other words, the lower stopping criterion, σ_D equal to 200 MPa at 10-km depth, might be sufficient for rifts faults with $\mu = 0.3$ or 0.4 to slip if pore fluid pressure is sufficiently high. Another possible consequences of pore fluid pressure is that faults could be reactivated at smaller angles from the maximum compressive stress (e.g., Chen & Chen, 2018).

4.4. Velocity Model of the CSZ

Our models show that a 1-D velocity model of the CSZ (Lamontagne, 1999; Figure 3) with embedded impact structure and rift faults can explain the observed seismicity and more than 50% of the stress rotations (Figure 12a). Using the velocity model of the Saguenay region does not improve this result (Figure 6). Similarly, $\Delta\sigma_D'$ in the TD70 model did not spatially fit the recorded earthquakes in the upper 10 km in the CSZ because the distinct and lower-strength damaged zone is not apparent in the 3-D tomography (Powell & Lamontagne, 2017; Figure 12b). Lamontagne (1999) constructed a 1-D velocity model for the Canadian Shield region that does not include lateral variations of velocity model to explain the seismicity and stress orientations.

4.5. Limitations of Our Study

Our models could not explain some earthquakes in the SW part of the impact structure especially in the upper 10-km depth (Figure 6c). We did not account for stress changes due to a large historic earthquake in the CSZ and the postglacial rebound as modeled by Fereidoni and Atkinson (2014) and Mazzotti et al. (2005), respectively.

Our models can only explain about 50% of the observed SH_{max} rotation. A possible hypothesis for the remaining stress rotation is a change in the dip of the rift faults with depth and the effect of postglacial rebound. Most of the focal mechanisms used for stress inversion in the CSZ are obtained from first motion P and SH waves (Lamontagne, 1998; Mazzotti & Townend, 2010). The focal mechanisms are well defined, and

we suggest that the focal mechanisms can be further constrained using waveform modeling to validate the magnitude of the stress rotation.

We assumed that the rift faults to be planar, however, the fault traces on the geologic map of the CSZ are not linear (Figure 1). The scatter of the seismicity within the impact structure indicates that the faults do not remain planar. Future models depicting a more realistic fault geometry may also shed light on the factors controlling stress rotation. Our model also did not incorporate pore pressure which could have affected the calculated μ and maximum σ_D. The 3-D velocity model is not very well defined in the upper 5-km depth and does not cover the entire seismic zone (Figure 4).

5. Conclusions

Findings from this study can be summarized as follows:

- The combined effects of the impact structure and the rift faults are required in the CSZ to explain the observed distribution of seismicity and more than 50% of the observed clockwise rotations of the ϕ_{max} in the CSZ with respect to the regional maximum compressive stress direction.
- An impact structure elastically weaker than the surrounding crust by up to a factor of 4 is required to explain the seismicity in the upper 10 km of the CSZ and the observed clockwise rotation of the SH_{max} in the SE relative to the NW part of the impact structure. Below 10-km depth in the impact structure, reactivation of the rift faults explains the observed seismicity in the CSZ.
- Stress models that spatially correlate with the seismicity of CSZ and the observed stress rotations were obtained when rifts faults have a friction coefficient of 0.3 and zero cohesion under an assumption of no pore fluid pressure on the rift faults.
- The magnitudes of SH_{max} rotation are greater in the 65°-40°-40° fault dip case than the constant 70° fault dip case by 6°. The remaining SH_{max} rotation could be due to a change in the dip of the rift faults with depth.
- Stress models with dips of 65°, 40°, and 40° based on a recent hypocenter relocation study show a better correlation between the high differential stress regions and the observed seismicity near and within the impact structure region than those with a constant 70° dip. However, the constant-dip models fit the observed seismicity better in the northeast region outside the impact structure. The partial success of each model might indicate more complex geometry of the faults: for example, an along-strike variation of the dip angles of the rift faults.

Acronyms

CSZ Charlevoix Seismic Zone.
SH_{max} Maximum horizontal principal stress.

Acknowledgments
This project is supported by the National Science Foundation (NSF-ICER) under the award title "EarthCube Building Blocks: Collaborative Proposal: GeoTrust: Improving Sharing and Reproducibility of Geoscience Applications" with Award 1639706. We acknowledge the high-performance computing (HPC) resource center at the University of Memphis, TN, for providing the computing time for this research. Earthquake data sets are available from Earthquakes Canada, GSC, Earthquake Search (On-line Bulletin), http://earthquakescanada.nrcan.gc.ca/stndon/NEDB-BNDS/bulletin-en.php, Natural Resources Canada (1/30/2019).

References

Aagaard, B., Kientz, S., Knepley, M. G., Strand, L., & Williams, C. (2015). PyLith user manual, Version 2.1.0. Computational Infrastructure of Geodynamic, Davis, CA.

Aagaard, B. T., Knepley, M. G., & Williams, C. A. (2013). A domain decomposition approach to implementing fault slip in finite-element models of quasi-static and dynamic crustal deformation. *Journal of Geophysical Research: Solid Earth*, *118*, 3059–3079. https://doi.org/10.1002/jgrb.50217

Anglin, F. M. (1984). Seismicity and faulting in the Charlevoix zone of the St. Lawrence Valley. *Bulletin of the Seismological Society of America*, *74*(2), 595–603.

Baird, A. F., McKinnon, S. D., & Godin, L. (2010). Relationship between structures stress and seismicity in the Charlevoix Seismic Zone revealed by 3-D geomechanical models: Implications for the seismotectonics of continental interiors. *Journal of Geophysical Research*, *115*, B11402. https://doi.org/10.1029/2010jb007521

Byerlee, J. (1978). Friction of rocks. *Pure and applied geophysics PAGEOPH*, *116*(4-5), 615–626. https://doi.org/10.1007/bf00876528

Chen, S., & Chen, Z. (2018). On the reactivation of the pre-existing normal fault. *World Journal of Mechanics*, *8*(5), 210–217. https://doi.org/10.4236/wjm.2018.85016

Fereidoni, A., & Atkinson, G. M. (2014). Correlation between Coulomb stress changes imparted by historic earthquakes and current seismicity in Charlevoix Seismic Zone, eastern Canada. *Seismological Research Letters*, *86*(1), 272. https://doi.org/10.1785/0220140134

Gardner, G. H. F., Gardner, L. W., & Gregory, A. R. (1974). Formation velocity and density—The diagnostic basics for stratigraphic traps. *Geophysics*, *39*(6), 770–780. https://doi.org/10.1190/1.1440465

Hurd, O., & Zoback, M. D. (2012a). Intraplate earthquakes, regional stress and fault mechanics in the central and eastern U.S. and southeastern Canada. *Tectonophysics*, *581*, 182–192. Crustal Stresses, Fractures, and Fault Zones: The Legacy of Jacques Angelier, https://doi.org/10.1016/j.tecto.2012.04.002

Hurd, O., & Zoback, M. D. (2012b). Regional stress orientations and slip compatibility of earthquake focal planes in the New Madrid Seismic Zone. *Seismological Research Letters*, *83*(4), 672. https://doi.org/10.1785/0220110122

Lamontagne, M. (1998). New and revised earthquake focal mechanisms for the Charlevoix Seismic Zone, Canada. Geological Survey of Canada. Open File, OF3556.

Lamontagne, M. (1999). Rheological and geological constraints on the earthquake distribution in the Charlevoix Seismic Zone, Quebec, Canada. Geological Survey of Canada. Open File, D3778.

Marone, C. (1995). Fault zone strength and failure criteria. *Geophysical Research Letters*, *22*(6), 723–726. https://doi.org/10.1029/95GL00268

Mazzotti, S., James, T. S., Henton, J., & Adams, J. (2005). GPS crustal strain, postglacial rebound, and seismic hazard in eastern North America: The Saint Lawrence Valley example. *Journal of Geophysical Research*, *110*, B11301. https://doi.org/10.1029/2004JB003590

Mazzotti, S., & Townend, J. (2010). State of stress in central and eastern North American seismic zones. *Lithosphere*, *2*(2), 76–83. https://doi.org/10.1130/l65.1

Powell, C. A., & Lamontagne, M. (2017). Velocity models and hypocenter relocations for the Charlevoix Seismic Zone. *Journal of Geophysical Research: Solid Earth*, *122*, 6685–6702. https://doi.org/10.1002/2017jb014191

Rondot, J. (1971). Impactite of the Charlevoix structure Quebec, Canada. *Journal of Geophysical Research*, *76*(23), 5414–5423. https://doi.org/10.1029/jb076i023p05414

Rondot, J. (1994). Recognition of eroded astroblemes. *Earth-Science Reviews*, *35*(4), 331–365. https://doi.org/10.1016/0012-8252(94)90001-9

Rondot, J. (2000). Charlevoix and Sudbury as gravity-readjusted impact structures. *Meteoritics & Planetary Science*, *35*(4), 707–712. https://doi.org/10.1111/j.1945-5100.2000.tb01454.x

Somerville, P. G., McLaren, J. P., Saikai, C. K., & Helmberger, D. V. (1990). The 25 November 1988 Saguenay, Quebec, earthquake: Source parameters and the attenuation of strong ground motion. *Bulletin of the Seismological Society of America*, *80*, 1118–1143.

Stevens, A. E. (1980). Reexamination of some larger La Malbaie, Qubec, earthquakes (1924–1978). *Bulletin of the Seismological Society of America*, *70*(2), 529–557.

Thomas, W. A., & Powell, C. A. (2017). Necessary conditions for intraplate seismic zones in North America. *Tectonics*, *36*, 2903–2917. https://doi.org/10.1002/2017TC004502

Vlahovic, G., Powell, C., & Lamontagne, M. (2003). A three-dimensional P wave velocity model for the Charlevoix Seismic Zone, Quebec, Canada. *Journal of Geophysical Research*, *108*(B9), 2439. https://doi.org/10.1029/2002JB002188

Yu, H., Liu, Y., Harrington, R. M., & Lamontagne, M. (2016). Seismicity along St. Lawrence paleorift faults overprinted by a meteorite impact structure in Charlevoix, Quebec, eastern Canada seismicity along St. Lawrence paleorift faults overprinted by a meteorite impact structure in Charlevoix. *Bulletin of the Seismological Society of America*, *106*(6), 2663. https://doi.org/10.1785/0120160036

Zoback, M. L. (1992). First- and second-order patterns of stress in the lithosphere: The world stress map project. *Journal of Geophysical Research*, *97*(B8), 11703. https://doi.org/10.1029/92JB00132